DOI: 10.1070/QEL16160

In loving memory of Valentin Georgievich Dmitriev

Functional possibilities of nonlinear crystals for laser frequency conversion: biaxial crystals

Yu.M. Andreev, Yu.D. Arapov, S.G. Grechin, I.V. Kasyanov, P.P. Nikolaev

Abstract. **We report the method and results of a complex analysis of phase-matching and nonlinear properties for biaxial crystals of all point groups of symmetry, which determine their functional possibilities in solving various problems of nonlinear frequency conversion of laser radiation.**

Keywords: *nonlinear optical crystals, frequency conversion, biaxial crystals.*

The technique for a complex analysis of the functional possibilities of nonlinear crystals in solving different problems of frequency conversion was reported in [1]. This technique is based on determining the dependence of the maximum value of the effective nonlinear coefficient d_{eff} along the phase-matching (PM) direction on the laser wavelengths in the range of crystal transparency. The presence of PM for the specified wavelengths and a value of d_{eff} belong to the main factors that determine the potential possibilities of a crystal in solving applied problems of laser radiation generation at sum and difference frequencies. The PM region and maximum d_{eff} values, which can be obtained for a given crystal, are determined for different combinations of wavelengths. These data allow one to find the wavelengths at which angular noncritical phase matching (ANCPM) and frequency-noncritical phase matching (FNCPM) occur. One of the advantages of the proposed method is the qualitative and quantitative determination of the functional possibilities of new crystals, the number of which constantly increases. In addition, this method makes it possible to perform an on-line comparison of the parameters of different crystals when solving practical problems. The results obtained by applying this method to uniaxial crystals of different point symmetry groups with interactions of all types were reported in [1]. In continuation of paper [1], we report similar results for biaxial crystals in this paper.

Yu.M. Andreev Institute of Monitoring of Climatic and Ecological Systems, Siberian Branch, Russian Academy of Sciences, Akademicheskii prosp. 10/3, 634055 Tomsk, Russia; Institute of High-Current Electronics, Siberian Branch, Russian Academy of Sciences, Akademicheskii prosp. 2/3, 634055 Tomsk, Russia;
Yu.D. Arapov, I.V. Kasyanov Russian Federal Nuclear Center, Zababakhin All-Russian Scientific Research Institute of Technical Physics, ul. Vasil'eva 13, POB 245, 456770 Snezhinsk, Chelyabinsk region, Russia;
S.G. Grechin, P.P. Nikolaev N.E. Bauman Moscow State Technical University, 2-ya Baumanskaya ul. 5, str. 1, 105005 Moscow, Russia; e-mail: gera@bmstu.ru

Received 16 June 2016
Kvantovaya Elektronika **46** (11) 995–1001 (2016)
Translated by Yu.P. Sin'kov

Currently, there are more than 20 biaxial nonlinear crystals of four point groups of symmetry that are most widely used in practice; they have a number of qualitative differences from uniaxial crystals. Table 1 contains a list of crystals and corresponding point symmetry groups. For uniaxial crystals, the relationship between the crystal-optical (CO) and crystal-physical (CP) coordinate systems remains the same in the entire range of transparency. The distribution $d_{\text{eff}}(\varphi,\theta)$ is determined by the form of the nonlinear susceptibility tensor d_{ijk} and the relations between its coefficients. For example, the uniaxial KDP crystal (point group $\bar{4}2$m) and crystals isomorphic to it are characterised by similar distributions $d_{\text{eff}}(\varphi,\theta)$ [1]. For BBO and $LiNbO_3$ crystals (point group 3m), the differences in the distributions $d_{\text{eff}}(\varphi,\theta)$ are due to the significant differences between the tensor coefficients d_{ij} [1].

In the case of biaxial crystals (Table 1), the relationship between the coordinate systems can be arbitrary in the entire transparency range. This feature is most pronounced, e.g., for the crystals belonging to the point group mm2. This relationship between the CP and CO systems leads to the following: the form of the $d_{\text{eff}}(\varphi,\theta)$ distribution in the CO coordinate system (in which all phase-matching properties of crystals are

Table 1.

Point group	Correspondence between the CO and CP coordinate systems	Crystal
	$XYZ \leftrightarrow abc$	BNN ($Ba_2NaNb_5O_{15}$), KB5 ($KB_5O_8{\cdot}4H_2O$), KTA ($KTiOAsO_4$), KTP ($KTiOPO_4$), RTA ($RbTiOAsO_4$), RTP ($RbTiOPO_4$), CTA ($CsTiOAsO_4$)
mm2	$XYZ \leftrightarrow acb$	LBO (LiB_3O_5)
	$XYZ \leftrightarrow bac$	KN ($KNbO_3$), LIS ($LiInS_2$), LISe ($LiInSe_2$), LGS ($LiGaS_2$) at $\lambda < 6.5$ μm, LGSe ($LiGaSe_2$) at $\lambda < 8$ μm
	$XYZ \leftrightarrow bca$	$MgBaF_4$, LGS ($LiGaS_2$) at $\lambda > 6.5$ μm, LGSe ($LiGaSe_2$) at $\lambda > 8$ μm
222	$XYZ \leftrightarrow bca$	α-Iodic Acid (α-HIO_3), LRB4 ($LiRbB_4O_7$)
	$XYZ \leftrightarrow cab$	CBO (CsB_3O_5)
2	$X\|\|b$, $Z\text{^}a = 31°$, $Y\text{^}c = 15.2°$	BIBO (BiB_3O_6)
	$Y\|\|b$, $Z\text{^}a = 46.03°$, $X\text{^}c = 47.5°$	LCB ($La_2CaB_{10}O_{19}$)
m	$Y\|\|b$, $Z\text{^}a = 27.2°$, $X\text{^}c = 19.2°$	GdCOB ($GdCa_4O(BO_3)_3$)
	$Y\|\|b$, $Z\text{^}a = 24.7°$, $X\text{^}c = 13.5°$	YCOB ($YCa_4O(BO_3)_3$)

Table 2. Distributions $d_{eff}(\varphi,\theta)$ for some biaxial crystals*.

Point group and correspondence between the CO and CP coordinate systems	Interaction type	
	ssf	fsf, sff
mm2 $XYZ \leftrightarrow abc$ (KTP)	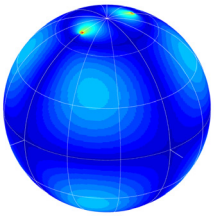	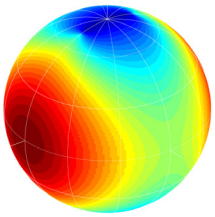
mm2 $XYZ \leftrightarrow acb$ (LBO)	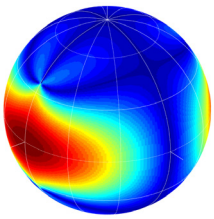	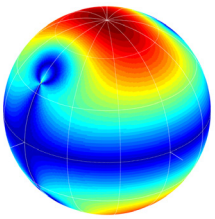
mm2 $XYZ \leftrightarrow bac$ (LIS)	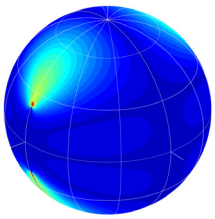	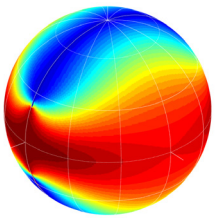
222 $XYZ \leftrightarrow cab$ (CBO)	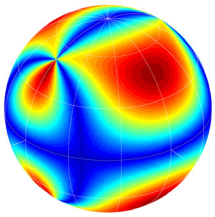	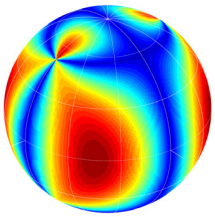

*All the distributions in Table 2 and Figs 1, 2, 4–7, 9, and 10 are presented in colour in the online version of Quantum Electronics.

traditionally considered) differs from that in the CP system; this is clearly evidenced by the data on the spatial distributions $d_{eff}(\varphi,\theta)$ for widely used biaxial crystals (Table 2).

In contrast to uniaxial crystals, which are classified (in correspondence with the difference in the principal values of refractive indices n_Z and $n_Y = n_Y$) as positive and negative, it is generally accepted to choose the CO system axes in biaxial crystals proceeding from the condition $n_Z > n_Y > n_Y$. Note that this condition is satisfied for the overwhelming majority of crystals in the entire spectral range of their transparency. However, there are some exceptions, where any of these inequalities may change to opposite with a change in wavelength.

The change in the signs in the inequality for refractive indices n_Z, n_Y, and n_X indicates that there is a wavelength at which some corresponding refractive indices are equal, and the crystal in fact becomes uniaxial: the angle V_Z between the optical axis and Z axis is zero (this is equivalent to the change in the mutual orientation between the CO and CP coordinate systems). For example, for the LGS ($LiGaS_2$) and LGSe ($LiGaSe_2$) crystals (see Table 1), the signs in the inequalities for the refractive indices change at wavelengths of 6.5 and 8 μm, respectively. We restrict our consideration to the crystals for which $n_Z > n_Y > n_X$.

Another specific feature of biaxial crystals is that the CP coordinate system for point groups 2 and m (which enter the monoclinic system) is not orthogonal, and the angles between the principal axes depend on both the wavelength and crystal temperature. This leads to the following. Biaxial crystals of point symmetry groups mm2 and 222, as well as all uniaxial crystals, have symmetry planes, a fact determining the symmetry of $d_{eff}(\varphi,\theta)$ distributions with respect to the principal crystal planes (XY, XY, and YZ). Therefore, the phase-matching and nonlinear properties are identical, e.g., for crystal cuts with φ_{phm} and $-\varphi_{phm}$ (in the XY plane, $\theta = 90°$). For crystals of point groups 2 and m, this does not hold true.

Figures 1 and 2 show the distributions of the crystal figure of merit $FOM_2 = d_{eff}^2/n^3$ (n is the refractive index), which characterises the frequency conversion for the ssf, sff, and fsf types of interaction with respect to intensity [2, 3] in some biaxial crystals. The calculations were performed using the data on the refractive index and nonlinear susceptibility tensor coefficients from [4].

The character of the distributions $FOM_2(\lambda_1,\lambda_2)$ is determined by the dispersion relation of the refractive indices and the point symmetry group of crystal. The solid lines are isolines of wavelength λ_3, which are obtained for a specified combination of λ_1 and λ_2 (λ_1, λ_2, and λ_3 are the wavelengths of the waves interacting during frequency conversion, $1/\lambda_1 + 1/\lambda_2 = 1/\lambda_3$). Hereinafter, the field beyond the spectral range of transparency and existence of phase matching is shown white for clearness. In view of the accepted relation $\lambda_1 \geqslant \lambda_2$, the distributions are given for the wavelengths lying below the line $\lambda_1 = \lambda_2$, which corresponds to the second-harmonic generation (SHG).

The dashed lines in Figs 1 and 2 show the transparency ranges of crystals, and the dot-dashed lines indicate the wavelength ranges, which were determined by the applicability limits of the derived Sellmeier equations. The peculiarity of the dependence $FOM_2(\lambda_1,\lambda_2)$ for the KTP crystal in the range of maximum wavelengths is obviously determined by the error of Sellmeier equations [5] in this range. The maximum (FOM_{2max}) values in the distributions $FOM_2(\lambda_1,\lambda_2)$ and the corresponding $d_{eff\,max}$ values are listed in Table 3.

Table 3. Maximum values $d_{eff\,max}$ and FOM_{2max} for some biaxial crystals.

Crystal	$d_{eff\,max}$/pm V^{-1}		FOM_{2max}/pm V^{-1}		
	ssf	fsf, sff	ssf	fsf	sff
KTP	0.87	3.3	0.171	2.628	2.625
LBO	0.85	0.784	0.177	0.117	0.115
LIS	4.8	6.2	1.946	3.503	3.328
CBO	1.08	1.08	0.303	0.328	0.327

Biaxial crystals are characterised by the same general properties of FOM_2 distributions as uniaxial crystals [1]: there are areas of maximum (FOM_{2max}) values in them. These areas are limited by both the ranges of transparency of crystals and the absence of phase matching ($\Delta k \neq 0$). For example, the largest FOM_2 values for the LBO crystal can be obtained for the interactions of ssf and sff types at SHG in the wavelength range of $\lambda_1 = \lambda_2 = 1.1–1.6$ μm and for the interactions of fsf type at sum-frequency generation (SFG) in the wavelength ranges of $\lambda_1 = 1.2–3.2$ μm and $\lambda_2 = 1.3–1.4$ μm. As in the case of uniaxial crystals, radiation with a minimum wavelength can be obtained at SFG for interactions of ssf and fsf types, and the PM area is minimum for the sff-type interaction.

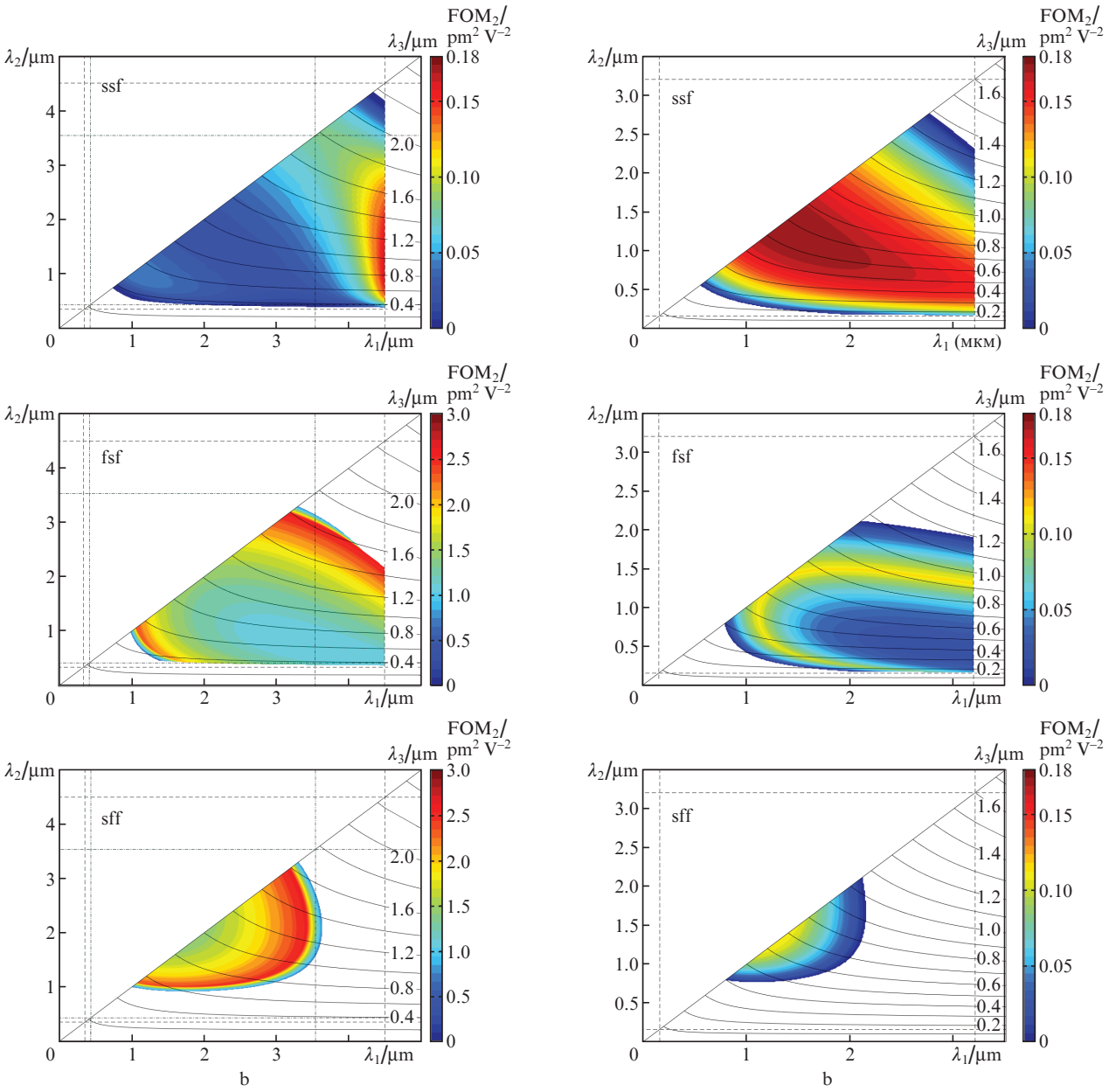

Figure 1. Distributions $\mathrm{FOM}_2(\lambda_1, \lambda_2)$ for (a) KTP (mm2, $XYZ \leftrightarrow abc$) and (b) LBO (mm2, $XYZ \leftrightarrow acb$) crystals.

All the crystals presented in Table 1 exhibit significant differences in the distributions $d_{\mathrm{eff}}(\varphi, \theta)$ (Table 2) and in maximum values $\mathrm{FOM}_{2\max}$ (Table 3) for the interactions of ssf and sff (fsf) types. The maximum values $d_{\mathrm{eff}\,\max}$ for these crystals in the case of the ssf-type interaction lie in the vicinity of the optical axis. However, $\mathrm{FOM}_{2\max}$ is determined by both the $d_{\mathrm{eff}\,\max}$ value and the possibility of implementing PM, the direction of which in the XZ plane should be closest to the area in which $d_{\mathrm{eff}\,\max}$ is implemented. For the LIS crystal, under the ssf-type interaction, the d_{eff} value in the vicinity of the optical axis is comparable with those for the interactions of the sff and fsf types. In this case, the $\mathrm{FOM}_{2\max}$ values are comparable for interactions of all types (Table 3). For the KTP crystal, the $d_{\mathrm{eff}\,\max}$ value is small in the vicinity of the optical axis, due to which $\mathrm{FOM}_{2\max}$ is also small (Table 3). In addition, $d_{\mathrm{eff}}(\varphi, \theta)$ for biaxial crystals, in contrast to uniaxial ones, depends on all wavelengths of the radiations interacting in the medium, because this distribution depends on the angle V_Z, the change in which is determined by the refractive index dispersion.

The significant difference between biaxial and uniaxial crystals manifests itself when ANCPM is implemented. ANCPM always occurs in the XY plane ($\theta = 90°$) for interactions of all types due to the axisymmetric distribution of the refractive index in uniaxial crystals. This situation is implemented at the combinations of wavelengths λ_1, λ_2, and λ_3 corresponding to the PM boundary.

The situation in biaxial crystals is different. For the ssf-type interaction, at the boundary of the wavelength range within which PM exists, ANCPM is always implemented along the Y axis [6–8]. The diagrams of PM directions, which indicate transitions between different PM distributions for interactions of all types, are presented in Fig. 3 [6]. The external boundary of the distribution contour for the ssf-type interaction in Fig. 1, as in the case of uniaxial crystals, corresponds to the ANCPM for this interaction. The character of change

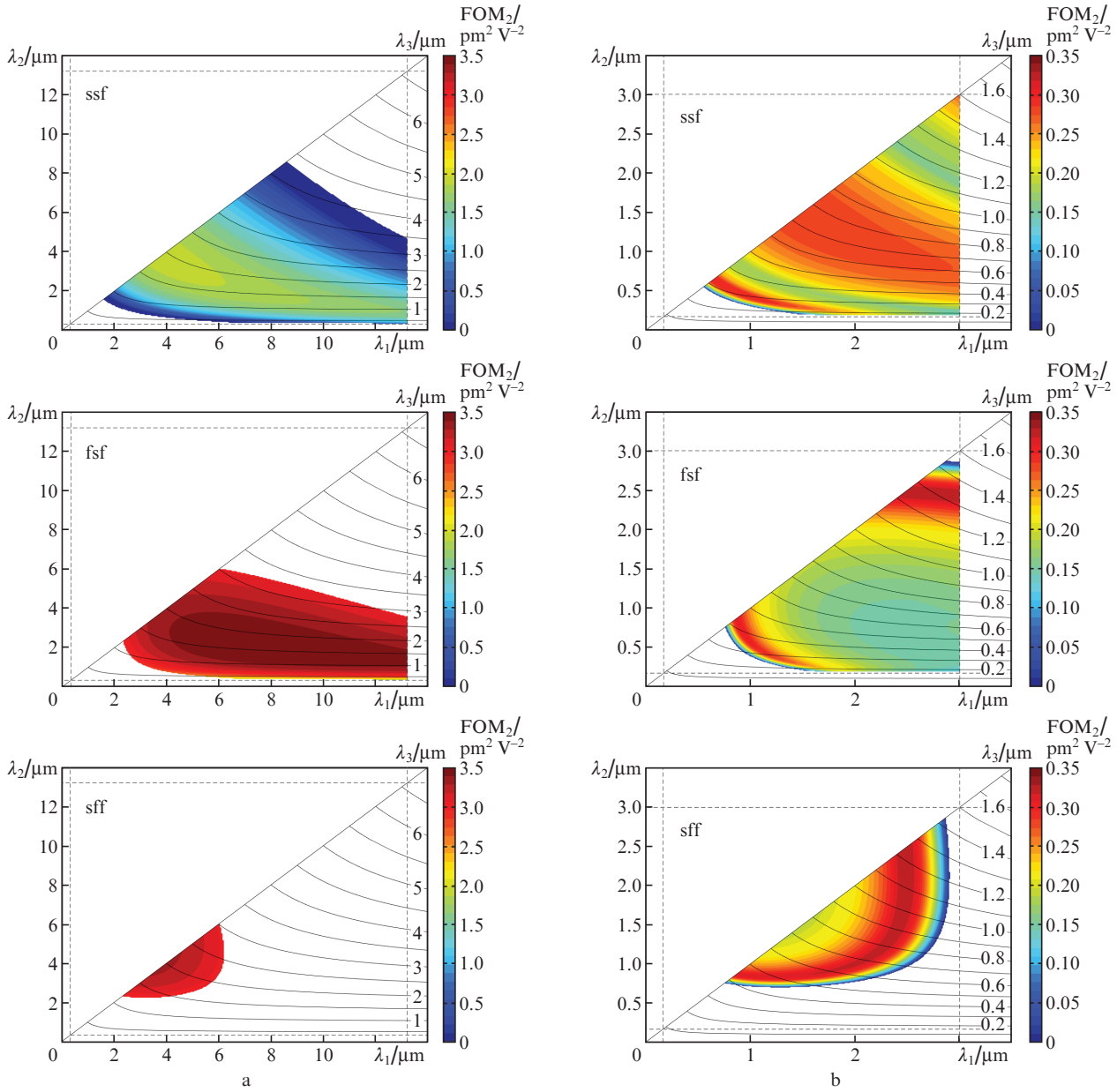

Figure 2. Distributions $\mathrm{FOM}_2(\lambda_1, \lambda_2)$ for (a) LIS (mm2, $XYZ \leftrightarrow bac$) and (b) CBO (222, $XYZ \leftrightarrow cab$) crystals.

in the cone of PM directions for the ssf-type interaction is such [6–8] that a change in wavelength results in successive implementation of ANCPM along the X axis (transition 0–1–2) or Z axis (transition 0–1–3) (Fig. 3a). These axes correspond to ANCPM. In principle, the ANCPM regime may exist simultaneously along these two axes (transition 0–1–4). When the PM direction passes from one principal axis to another, the PM is critical along one angular coordinate and noncritical along the other, and the angular PM widths are different [9].

For the interactions of the sff and fsf types, ANCPM may occur at the boundary of the PM range along both the principal axis Y (transition 0–1) and the principal axis X (transition 0–5) (Fig. 3b). This possibility is determined by the relations between the refractive indices even when the condition $n_Z > n_Y > n_X$ is satisfied [6–8]. If PM arises along the X axis, a further change in wavelengths λ_1 and λ_2 leads to its successive implementation along the Y axis (transition 0–5–2,

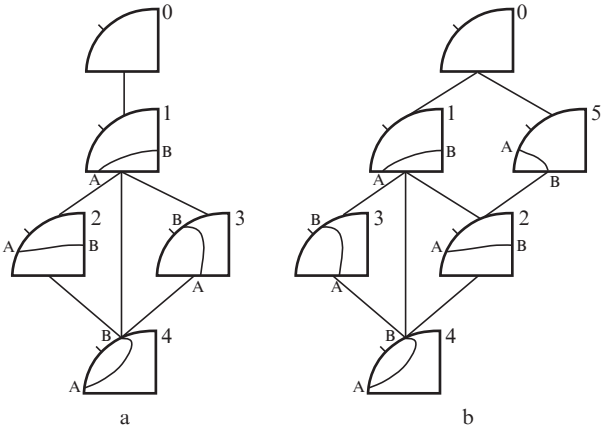

Figure 3. Main configurations of PM directions for the (a) ssf and (b) fsf and sff types of interaction [6–8].

Fig.3b) and then along the Z axis (transition 2–4, Fig. 3b). If PM arises along the Y axis, the character of the transitions is similar to that occurring for the ssf-type interaction. However, it should be noted that the occurrence of PM at one of the boundaries of its range (along the X or Y axis) does not indicate that it will occur in the same order at the other boundary of the PM range (possible transitions are 0–5–2–1–0, 0–5–2–4–1–0, or 0–5–2–4–3–0) [6–8].

Let us consider all aforesaid by the example of the LBO crystal. Figure 4 presents the dependences determining the λ_1 and λ_2 values at which ANCPM is implemented for the ssf-type interaction along the X axis at different temperatures of LBO crystal. The conservation of the PM direction along the X axis with a change in wavelength is in agreement with the transitions in the diagram in Fig. 3a. An increase in temperature leads to a significant change in the combinations of wavelengths at which ANCPM occurs. The dashed lines in Fig. 4, which intersect the λ_1 and λ_2 axes at the points $\lambda_1 = \lambda_2 = 1.0642$ μm (SHG), and the point of their intersection correspond to the implementation of ANCPM for the ssf-type interaction, which is widely used in practice. The distributions $d_{\text{eff}}(\varphi,\theta)$ and PM directions corresponding to this case are shown in Fig. 5.

Figure 6 shows the dependence determining the λ_1 and λ_2 values at which ANCPM is implemented in the LBO crystal

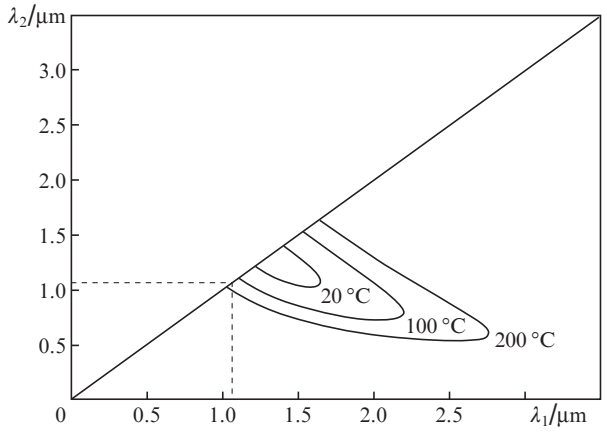

Figure 4. Dependences determining the λ_1 and λ_2 values at which ANCPM is implemented for the ssf-type interaction along the X axis at different temperatures of LBO crystal.

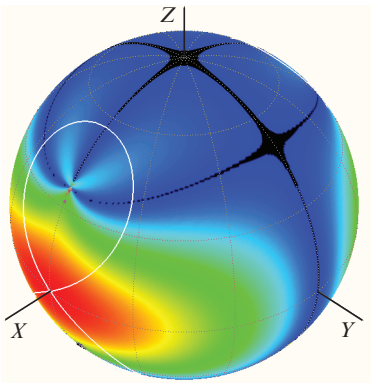

Figure 5. Distributions $d_{\text{eff}}(\varphi,\theta)$ and PM directions for the ssf-type interaction under ANCPM along the X axis in LBO crystal.

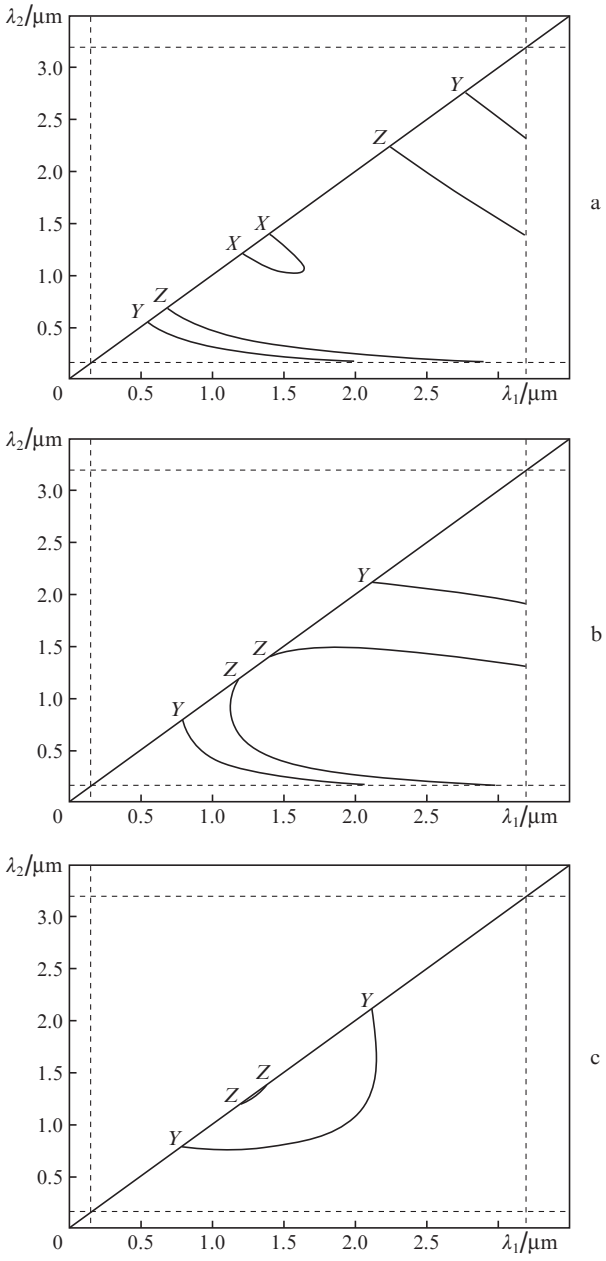

Figure 6. ANCPM for the interactions of (a) ssf, (b) fsf, and (c) sff types along all principal axes in LBO crystal at room temperature.

for interactions of all types at room temperature. In the entire range of variation in wavelength for the ssf-type interaction, PM arises at SHG ($\lambda_1 = \lambda_2$) along the Y axis ($\lambda_1 = \lambda_2 = 0.554$ μm), then along the Z axis ($\lambda_1 = \lambda_2 = 0.687$ μm), then along the X axis ($\lambda_1 = \lambda_2 = 1.212$ and 1.408 μm), then along the Z axis ($\lambda_1 = \lambda_2 = 2.2888$ μm), and again at the boundary along the Y axis ($\lambda_1 = \lambda_2 = 2.913$ μm). This situation corresponds to the 0–1–3–4–3–1–0 transitions in Fig. 3a. Generally, ANCPM cannot be implemented along the X axis. The wavelength range of the ANCPM regime is maximal at SHG. For the fsf-type interaction, ANCPM is absent along the X axis. A similar situation occurs for the sff-type interaction; however, in this case, the ANCPM occurs along the Z axis in a limited wavelength range.

The joint distributions $\text{FOM}_2(\lambda_1, \lambda_2)$ and the λ_1 and λ_2 values at which ANCPM is implemented for all PM types in LBO crystal are presented in Fig. 7. The distributions $d_{\text{eff}}(\varphi,\theta)$

for the ssf-type interaction (Table 2) show that there is maximum value $d_{\text{eff max}}$ along the X axis; the ANCPM regime is of greatest practical interest for specifically this direction. ANCPM is implemented in a fairly wide wavelength range. For the interactions of sff and fsf types, $d_{\text{eff max}}$ is obtained along the Z axis (see Table 2), in correspondence with the ANCPM direction. The change in the PM directions for the fsf-type interaction with a change in wavelength occurs between the elements in Fig. 3b in the following sequence: 0–1–3–1–0. Hence, $\text{FOM}_{2\text{max}}$ corresponds to the ANCPM regime in the $\text{FOM}_2(\lambda_1, \lambda_2)$ distribution. This can clearly be seen in Fig. 7b. The transitions for the sff-type interaction are similar to the fsf-type transitions in the diagram in Fig. 3b; however, the transition to element 3 occurs only in the wavelength range of 1.193–1.397 μm (Fig. 7c), within which ANCPM can be implemented. For the interactions of these two types, ANCPM is absent along the X axis, while the ANCPM along the Y axis is of no practical interest, because $d_{\text{eff}} = 0$ in this case.

The dispersion relations for $\text{FOM}_2(\lambda_1, \lambda_2)$ make it possible to determine the occurrence of FNCPM. In uniaxial crystals, it is implemented at a fixed wavelength, when the PM angle θ_{phm} is minimum [extremum in the dependence $\theta_{\text{phm}}(\lambda_1, \lambda_2)$]. On the whole, a similar situation is implemented for biaxial crystals. When passing over elements in the diagram in Fig. 3, starting from element 0 (PM is absent), some limiting distribution of PM directions is implemented, which is followed by the reverse transition to the initial element. In view of the symmetry of the distributions of PM directions and $d_{\text{eff}}(\varphi, \theta)$ with respect to the principal planes of crystal, there is an extreme value d_{eff} (corresponding to FNCPM) in one of the principal planes.

The wavelength dependences of the PM direction for the ssf-type SHG in the vicinity of the X axis for the LBO crystal are presented in Fig. 8. With an increase in wavelength from the UV boundary to the IR boundary of the transparency range, the PM directions undergo the following transition between configurations (Fig. 3): 0–1–3–4–3–1–0. Distribution 3 (see Fig. 3a) corresponds to two ranges: $\lambda \leqslant 1.21$ μm and $\lambda \geqslant 1.41$ μm. When the wavelength reaches these limiting values, the PM is directed along the X axis. This is the ANCPM regime. Within the range $1.21 \leqslant \lambda \leqslant 1.41$ μm, PM occurs in the XZ plane ($\varphi = 0$), a situation corresponding to distribution 4 in Fig. 3a. Here, FNCPM is implemented at a wavelength of 1.307 μm, which corresponds to the minimum value of angle θ: 86.2°.

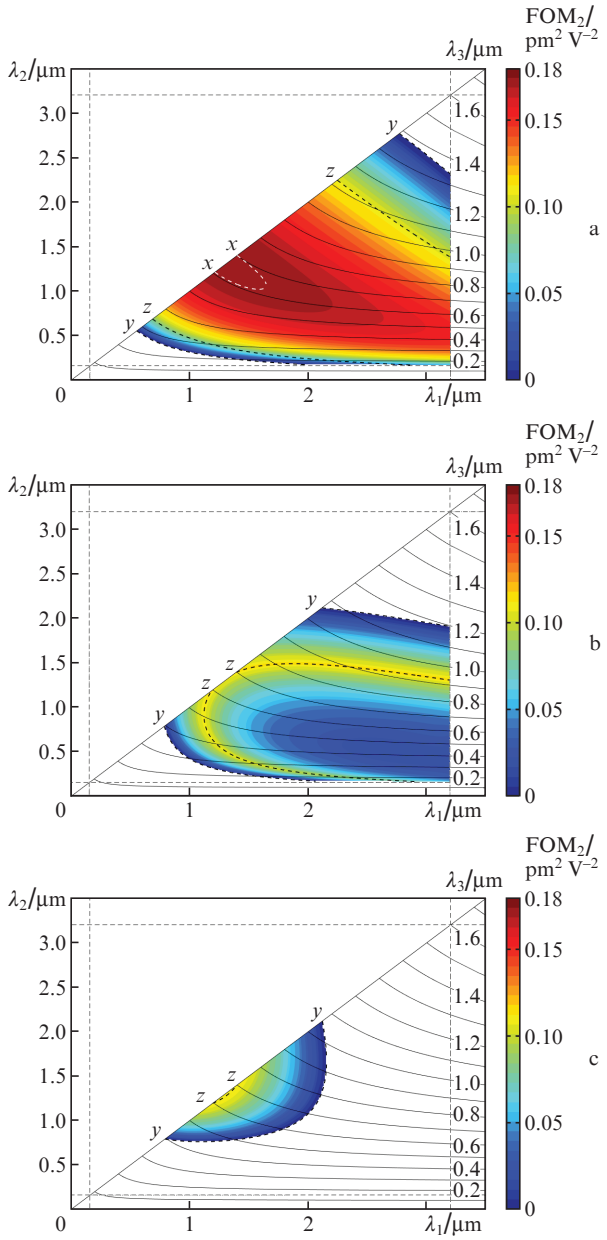

Figure 7. Distributions $\text{FOM}_2(\lambda_1, \lambda_2)$ and the dependences determining the λ_1 and λ_2 values at which ANCPM is implemented for the interactions of (a) ssf, (b) fsf, and (c) sff types (LBO crystal).

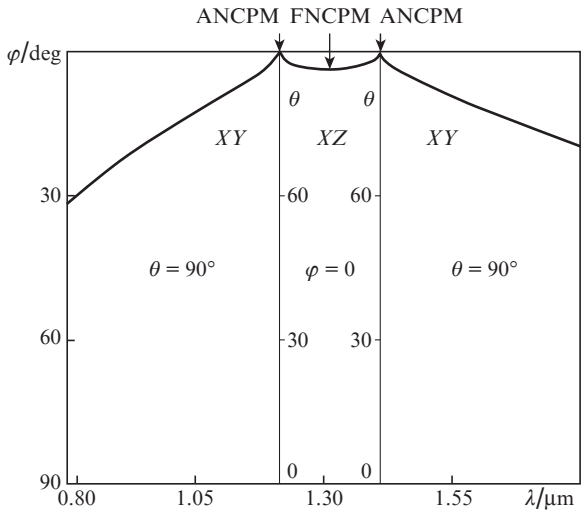

Figure 8. PM directions at SHG for the ssf-type interaction in LBO crystal.

Figure 9 shows the distributions of d_{eff} and PM directions for the ssf-type interaction in the case of SHG at $\lambda = 1.31$ μm (FNCPM) in the LBO crystal. Here, $\varphi_{\text{phm}} = 0$, $\theta_{\text{phm}} = 86.7°$, and the spectral PM width is 80.3 nm cm$^{1/2}$.

Note that, in contrast to uniaxial crystals, in which FNCPM may occur only at one fixed wavelength, biaxial crystals are characterised by a wavelength range within which this regime may exist (with a corresponding change in the PM angle). A theoretical analysis of the possibility of implementing FNCPM for biaxial crystals of all point groups was performed in [10].

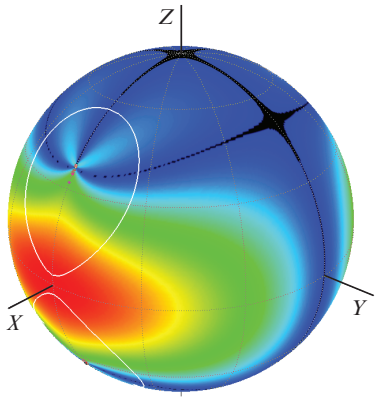

Figure 9. PM directions and distribution of d_{eff} for LBO crystal (ssf-type interaction) at SHG (wavelength 1.34 μm).

In the case of FNCPM in a certain direction (φ_{phm}, θ_{phm}), the PM condition is retained in a wide wavelength range. The d_{eff} value also remains invariable. Therefore, the isolines of the $\text{FOM}_2(\lambda_1, \lambda_2)$ distribution determine the wavelengths for which FNCPM will be implemented. The most descriptive illustration is the distribution $\text{FOM}_2(\lambda_1, \lambda_2)$ in Fig. 10. The solid straight lines are the dependences for the processes of conversion with multiple wavelengths (frequencies), at which the FNCPM regime is indicated by dots: generation of (A) second, (B) third, (C) fourth ($\omega_1 + 3\omega_1$), and (D) fifth ($\omega_1 + 4\omega_1$) harmonics. The maximum values along these straight lines correspond to the FNCPM regime for these processes. In more general cases of generation at sum and difference frequencies, the tangents to the $\text{FOM}_2(\lambda_1, \lambda_2)$ isolines show possible non-multiple values of λ_1 and λ_2 for implementing FNCPM.

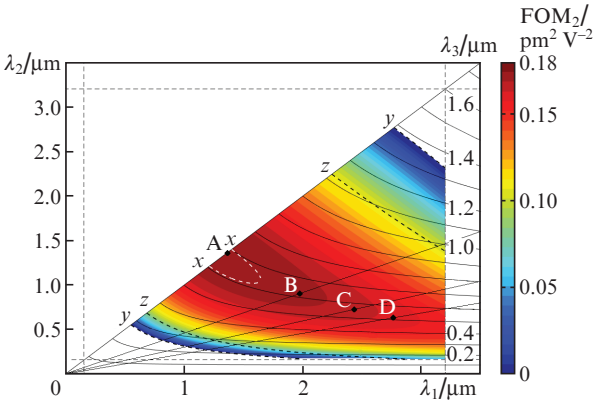

Figure 10. Distribution $\text{FOM}_2(\lambda_1, \lambda_2)$ for the ssf-type interaction in LBO crystal and the dependences determining the λ_1 and λ_2 values at which FNCPM is implemented for different processes of frequency conversion.

Similar to uniaxial crystals [1], SFG of ultrashort pulses in the field of quasi-steady-state radiation can also be implemented in biaxial crystals. It occurs when $\text{d}\,\text{FOM}_2(\lambda_1, \lambda_2)/\text{d}\lambda_i = 0$ with respect to one of the wavelengths λ_i, with a fixed value for another wavelength. The points in Fig. 11 indicate two particular cases of ultrashort pulse generation: (A) at λ_1 and (B) at λ_2. For case A, at $\lambda_2 = 0.54$ μm and $\lambda_1 = 2.7$ μm, the PM spectral width $\Delta\lambda_1 = 289.6$ nm cm$^{1/2}$ ($\lambda_3 = 0.45$ μm) and for case B, at $\lambda_1 = 2.15$ μm and $\lambda_2 = 0.81$ μm, the PM spectral width $\Delta\lambda_2 = 100.6$ nm cm$^{1/2}$ ($\lambda_3 = 0.588$ μm). The difference

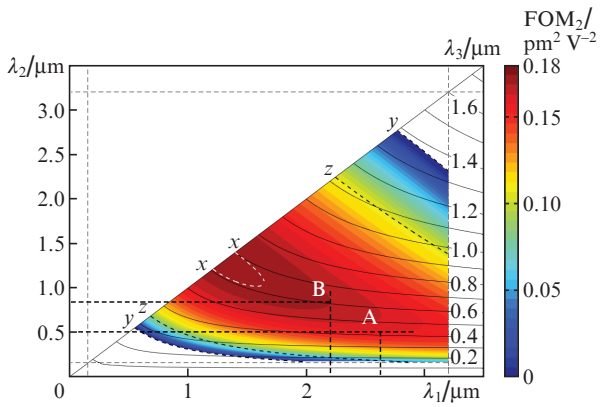

Figure 11. Distribution $\text{FOM}_2(\lambda_1, \lambda_2)$ for the ssf-type interaction in LBO crystal, which demonstrates possibility of generating ultrashort pulses in the field of quasi-steady-state radiation.

in the PM widths stems from the general character of change in the $\text{FOM}_2(\lambda_1, \lambda_2)$ distribution over λ_1 and λ_2.

On the whole, it follows from the results presented in Fig. 11 that the ultrashort pulse generation in the field of quasi-steady-state radiation may occur in a wide wavelength range (in the major part of the PM region), when there is a tangent to the $\text{FOM}_2(\lambda_1, \lambda_2)$ distribution over one laser wavelength at a fixed value of the other wavelength.

Thus, a technique of representing results for the complex analysis of PM and nonlinear properties of crystals in order to determine their functional possibilities in frequency conversion problems and perform a comparative analysis of different media when solving a number of applied tasks was proposed in [1] and in this study. The results obtained show that processes of frequency conversion under ANCPM and FNCPM conditions can also be studied. The general results for the four most popular crystals were reported, and the properties of the LBO crystal were analysed in detail. This technique can be used to investigate other biaxial crystals.

Acknowledgements. This work was supported by the Russian Foundation for Basic Research (Grant No. 15-02-07760). In the part related to the systematisation and interpretation of results, Yu.M. Andreev acknowledges the support of the Russian Science Foundation (Grant No. 15-19-10021).

References

1. Andreev Yu.M., Arapov Yu.D., Grechin S.G., Kas'yanov I.V., Nikolaev P.P. *Kvantovaya Elektron.*, **46**, 33 (2016) [*Quantum Electron.*, **46**, 33 (2016)].
2. Dmitriev V.G., Tarasov L.V. *Prikladnaya nelineinaya optika* (Applied Nonlinear Optics) (Moscow: Fizmatlit, 2004).
3. Grechin S.G. *Kvantovaya Elektron.*, **39**, 171 (2009) [*Quantum Electron.*, **39**, 171 (2009)].
4. Dmitriev V.G., Gurzadyan G.G., Nikogosyan D.N. *Handbook of Nonlinear Optical Crystals* (Berlin: Springer, 1999).
5. Kato K., Takaoka E. *Appl. Opt.*, **41**, 5040 (2002).
6. Fève J.P., Boulanger B., Marnier G. *Opt. Commun.*, **99**, 284 (1993).
7. Grechin S.G., Grechin S.S., Dmitriev V.G. *Kvantovaya Elektron.*, **30**, 377 (2000) [*Quantum Electron.*, **30**, 377 (2000)].
8. Huang J.J., Shen T., Ji G.J., Gao W., Wang H., Andreev Yu.M., Shaiduko A.V. *Opt. Commun.*, **281**, 3208 (2008).
9. Grechin S.G. *Kvantovaya Elektron.*, **40**, 822 (2010) [*Quantum Electron.*, **40**, 822 (2010)].
10. Grechin S.G., Grechin S.S. *Kvantovaya Elektron.*, **36**, 45 (2006) [*Quantum Electron.*, **36**, 45 (2006)].